Materials Horizons

ROYAL SOCIETY OF CHEMISTRY

COMMUNICATION

View Article Online
View Journal | View Issue

Cite this: *Mater. Horiz.*, 2025, **12**, 862

Received 15th August 2024,
Accepted 5th November 2024

DOI: 10.1039/d4mh01085j

rsc.li/materials-horizons

Transformation study and characterization of Cu-BTC MOF-derived nanoporous copper oxide†

Sameh Khalil, Abhijit Ganguly, Davide Mariotti and Supriya Chakrabarti *

This study provides a systematic and comprehensive investigation of the transformation process of copper-based metal–organic frameworks (Cu-BTC MOFs) into nanoporous copper oxides (P-CuO_x) through controlled calcination. While calcination is a well-established method for producing MOF-derived oxides, previous studies have primarily focused on their applications. Most of them often lack detailed exploration of the transformation process and decomposition mechanisms though it is crucial for achieving tunability in MOF-derived structures. Our study addresses this gap by offering valuable insights that can guide the production of various MOF-derived oxides with tunable structural and functional properties. In this report, we have meticulously analysed the combined effects of calcination parameters, including temperature (250–500 °C), heating rate (0.5–10 °C min^{-1}), and duration (1 and 2 hours) on the phase transformation, morphological features, and optical properties of Cu-BTC during its transformation to P-CuO_x. Results revealed that fine adjustments to these calcination parameters allow precise control over phase purity, surface area, and porosity, achieving a high surface area of 113 m^2 g^{-1} for derived P-CuO. Furthermore, the P-CuO_x materials exhibited strong visible-light absorption, highlighting their potential for solar energy harvesting applications. This approach opens opportunities for designing advanced materials with customized performance characteristics. The findings have broad applicability and enable the research community to fully exploit MOF-derived oxides for designing advanced materials with customized properties for diverse applications, including energy, sensing, and biomedical.

New concepts

In this study, we introduce a systematic exploration of the transformation of Cu-BTC metal–organic frameworks (MOFs) into nanoporous copper oxides (P-CuO_x) *via* controlled calcination, filling a significant gap in the understanding of the MOF-to-metal oxide transformation process. Unlike previous studies that have predominantly focused on applications of MOF-derived oxides, our research delves into the intricate transformation mechanism itself. By fine-tuning calcination parameters, including temperature, heating rate, and duration, we demonstrate precise control over phase purity, surface area, porosity, and optical absorption properties. This approach has not only allowed us to synthesize P-CuO_x with tunable properties but also provided new insights into the decomposition mechanism of Cu-BTC, setting a foundation for further exploration into material design with specific applications in mind. Moreover, our findings offer a broader framework for applying this novel calcination strategy to other metal–organic frameworks (MOF), potentially revolutionizing the design and functionality of materials across various high-efficiency applications.

1. Introduction

Nanoporous materials, which are characterized by their intricate networks of tiny pores, have emerged as a revolutionary class of materials with a wide range of applications.[1] These materials, with pores on the nanoscale, offer unique environments for interactions with molecules, atoms, and ions at multiple interfaces, both external and internal surfaces. Such interactions can lead to superior performance compared to their non-porous counterparts.[2,3] Among these materials, nanoporous metal oxides (P-MO_x) are of great importance, combining the benefits of metal oxide chemistry with the distinct features of porous structures. Such materials have a myriad of applications such as energy storage,[4] electrocatalysis, supercapacitors,[5,6] battery electrode materials,[7] sensing,[8,9] drug delivery applications.[10] However, synthesizing these P-MO_x with precise control over pore size, pore distribution, and structural hierarchy remains a significant challenge.

Metal–organic frameworks (MOFs) which are recognized as porous coordination polymers (PCPs) have received a great attention. MOFs are increasingly utilized as templates or precursors to derive P-MO_x with tuneable properties in simple one or two step processes. This is particularly important when considering the limitations and complexity of conventional

School of Engineering, Ulster University, York St, Belfast BT15 1AP, UK.
E-mail: s.chakrabarti@ulster.ac.uk

† Electronic supplementary information (ESI) available. See DOI: https://doi.org/10.1039/d4mh01085j

synthesis methods of P-MO_x such as soft-template, hard-template, electrospinning, and hydrothermal methods, which often struggle with uncontrollable pore size, limited oxide-types, and time consuming post-treatments.[11–14] Moreover, MOFs templated synthesis of P-MO_x provides versatility in producing single or multi-metal oxides with controlled structure, morphology, porosity and pore size distribution.[15,16]

The synthesis of MOF-derived metal oxides can be achieved primarily through two techniques: heat treatment[17] or chemical solution reactions.[18] Heat treatment is notably favoured in the synthesis of MOF-derived P-MO_x due to its simplicity and effectiveness. This method provides extensive control over the final properties of the derived metal oxides, including morphology, composition, and porosity. Such control is critical and is influenced by several factors: the choice of MOF precursor, the atmosphere during heating, and specific calcination parameters such as temperature, duration, and heating rate.[19] These factors collectively determine the quality and applicability of the synthesized P-MO_x. Also, the heat treatment process offers a rapid and sustainable route to transform MOFs into P-MO_x through a one-step procedure, with a higher degree of flexibility. This method's flexibility allows for the synthesis of a wide variety of metal oxides with tailored properties to suit specific applications.

Despite these advantages, achieving precise control over this thermal transformation process requires a deep understanding of the decomposition mechanisms of MOFs under heat. This area remains underexplored, especially regarding the detailed phase transitions and chemical changes that occur during heat treatment under varying parameters. Gaining comprehensive understanding could significantly expand the synthesis capabilities, enabling the precise tuning of compositions needed for diverse applications ranging from catalysis to energy storage. Success here could enhance the synthesis of a broad range of MOF-derived metal and enable compositional tuning as required for various applications.

Herein, a systematic study investigated the transformation of Cu-based MOF (Cu-BTC) into nanoporous copper oxides (P-CuO_x) under various thermal conditions, focusing on how calcination temperature (T_C), heating rate (HR), and duration influence the composition, porosity, and crystalline phases. Previous studies showed the formation of copper oxides from Cu-BTC and mostly focused on the applications of those derived materials.[20–24] In contrast, this work uniquely examines the transformation mechanism itself, revealing how precise adjustments to calcination parameters can control the phase purity, morphology, and pore size distribution. The findings revealed that both the T_C and HR significantly influence the phase transformations and porosity of the obtained P-CuO_x. At 300 °C, a critical T_C threshold was observed, where Cu-BTC transformed into mixed phases of CuO and Cu_2O, with the proportion of Cu_2O decreasing as the HR increased. Notably, slower HR favoured the maintenance of higher surface areas, with the highest recorded surface area of 113 $m^2\ g^{-1}$ achieved for P-CuO_x sample synthesized at T_C of 300 °C using a HR of 0.5 °C min^{-1} for 1 h. Higher T_C led to the complete transformation into a pure CuO phase. Furthermore, employing a step heating process demonstrated that a gradual increase in temperature can help optimize the surface area. The obtained P-CuO showed superior optical absorption over broader wavelength range with high intensity across the visible light range. These findings not only highlight the potential for precisely tailoring the properties of the synthesis of P-CuO_x required for specific application but also deepen the understanding of the Cu-BTC transformation process and how calcination parameters affect the structure and physicochemical properties of P-CuO_x.

2. Experimental work

2.1. Raw materials

Copper benzene-1,3,5-tricarboxylate (Cu-BTC) with empirical formula of $C_{18}H_6Cu_3O_{12}$, supplied by Sigma Aldrich, catalogue number 688614, was used as a precursor to derive P-CuO_x. The Cu-BTC crystalline structure was presented in Fig. S1 (ESI,† Section S1). Ethanol was employed as the dispersion medium for sample preparation for different characterization techniques and used as a base-fluid to prepare the dispersions for optical measurements.

2.2. Synthesis of P-CuO_x from Cu-MOF

Cu-BTC was employed as a precursor for synthesis of P-CuO_x through a carefully controlled heat treatment process conducted in a muffle furnace. The experiments were carried out in air environment under different heating parameters including calcination temperature (T_C), heating rate (HR), and duration. The schematic (Fig. 1) illustrates the calcination processes, highlighting how specific calcination parameters influence the formation of copper oxides derived from Cu-BTC. In each experimental setup, a precise quantity of 30 mg of Cu-BTC was uniformly spread across a 60 mm diameter borosilicate glass 3.3 Petri dish, which was then placed inside the furnace. The calcination process was executed at incremental T_C of 250, 300, 400, and 500 °C. This gradation allowed for a detailed analysis of temperature impacts on the transformation processes of the Cu-BTC. Further, to understand the influence of heating dynamics on the transformation process, this calcination process was carried out primarily with two HR: 5 °C min^{-1} and 1 °C min^{-1}, with each rate applied for durations of 1 and 2 hours. These variations were critical in determining the time-dependent effects on the synthesized P-CuO_x.

Specific attention was directed towards the samples calcinated at 300 °C, following intriguing phase composition findings from initial characterization results. These samples were subjected to further experimentation by applying the heat treatment with various HR (0.5, 1, 2, 3, 5, and 10 °C min^{-1}), each for 1 h. Moreover, a novel two-step calcination process was also employed. Initially, Cu-BTC was heated from room temperature to 300 °C at a rate of 1 °C min^{-1} and maintained at that temperature for 1 h. Subsequently, the temperature was raised to 500 °C at the same rate and held for an additional hour. To quantify the weight loss and further understand the transformation of Cu-BTC into P-CuO_x, each sample was

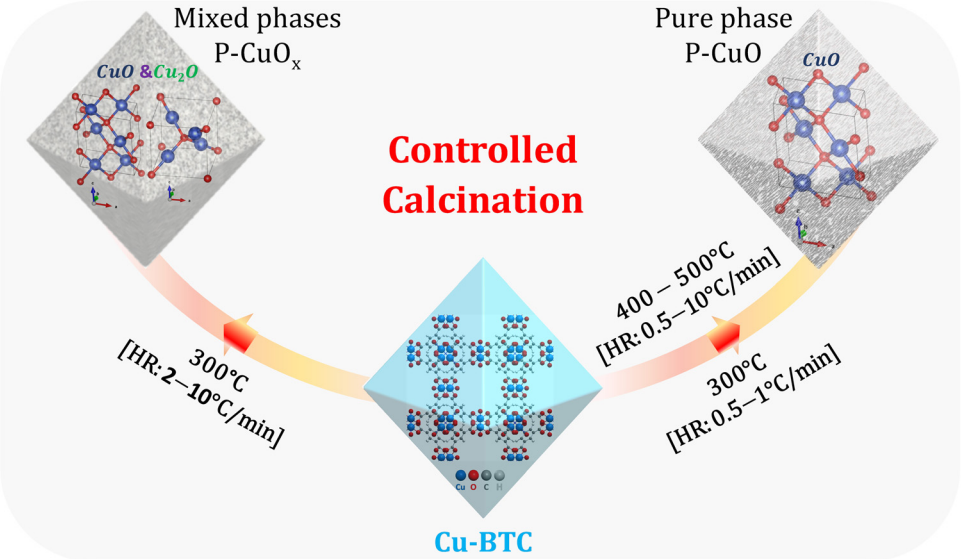

Fig. 1 Schematic illustrating the controlled calcination process of Cu-BTC driving the formation of copper oxides.

weighted before and after the calcination process. Finally, the obtained P-CuO$_x$ was analyzed for its chemical composition, morphology, related surface area, pore size, and optical properties.

2.3. Characterization

Morphological characteristics and chemical composition were examined using a HITACHI SU5000 scanning electron microscope (SEM) equipped with an energy-dispersive X-ray spectrometry (EDX) detector. SEM images were captured at an acceleration voltage of 10 kV. Samples were prepared *via* drop-casting, where the powder suspended in ethanol was placed on a silicon substrate and dried at 75 °C on a hot plate. Transmission electron microscope (TEM) measurements were performed at 200 kV using JOEL JEM-2100F. For TEM, a droplet of the ethanol-powder mixture was applied onto a copper-coated carbon grid and left to dry overnight. Crystallographic structures were characterized using X-ray diffraction (XRD) with a D8-Discover/Bruker diffractometer (Cu-Kα_1, λ = 1.54056 Å) at 40 kV/40 mA. XRD patterns were recorded over the 2θ range of 20–60° for P-CuO$_x$ powder samples loaded onto a zero-background substrate. Additionally, Raman spectroscopy was performed on P-CuO$_x$ powder samples placed on silicon substrate, using the Renishaw Invia Qontor system with a green laser as the excitation source at 532 nm. Thermogravimetric analysis (TGA) was performed using the TGA Q500 to investigate the weight loss occurring as a function of the temperature during the calcination process.

Surface and chemical bonding studies were conducted with X-ray photoelectron spectroscopy (XPS), reflection electron energy loss spectroscopy (REELS), and ultraviolet photoelectron spectroscopy (UPS) using the Thermo Fisher Scientific ESCALAB Xi$^+$ spectrometer. The spectrometer equipped with X-ray source of Al Kα anode ($h\nu$ = 1486.6 eV, 650 µm spot size), operated at 15 kV and 15 mA. Survey scans were recorded with step size of 1 eV and pass energy of 160 eV, while the high-resolution scans used a step size of 0.05 eV and pass energy of 20 eV. The operating pressure was maintained at 10^{-9} bar for all experiments. Thermo Scientific™ Avantage software was used for XPS fitting, referencing the adventitious carbon C–C peak at 284.8 eV for binding energy calibration. REELS were performed using a primary electron beam with an energy level of 1000 eV. Additionally, the electronic structure of P-CuO$_x$ was analyzed by UPS where the energy of monochrome UV light source was 21.22 eV. All measurements for XPS, REELS, and UPS were carried out on the same sample, prepared similarly to SEM samples. The Brunauer–Emmett–Teller (BET) specific surface area and pore volume characteristics were studied from the results of the nitrogen adsorption and desorption isotherms using the Nova-600, Anton Paar instrument with nitrogen as the adsorbate at 77 K and helium mode for void volume correction. Samples were first degassed at 130 °C for 16 hours to remove adsorbed gases and moisture, then weighed post-degassing before BET analysis.

Finally, ultraviolet-visible-near infrared (UV-Vis-NIR) spectroscopy was conducted to investigate the optical properties of the samples. Measurements were carried out at room temperature using the Lambda 1050+ with 150 mm integrating sphere, from PerkinElmer Inc. Liquid samples were prepared by dispersing the heat-treated Cu-BTC in ethanol. The process of achieving a homogeneous solution involved using a water bath sonication technique for 10 minutes. This method ensures well dispersion of the heat-treated Cu-BTC within the ethanol and is more suitable for maintaining, as closely as possible, the inherited engineering structure. Transmission and scattering measurements were conducted using three milliliters of the solution placed into a quartz cuvette, characterized by four clear-windows and 10 mm path length. The measurements were performed in both standard transmittance mode and using an integrating sphere, which recorded not only transmitted light but also any reflected or scattered light.

3. Results and discussion

3.1. X-ray diffraction study of MOF derived P-CuO_x

Comprehensive XRD analyses were conducted to assess phase transitions and crystallite size variations in Cu-BTC subjected to various calcination conditions. The XRD patterns, captured across a 2θ range of 20–60°, demonstrated notable phase evolution influenced by both calcination temperature (T_C) and the applied heating rate (HR). Initial examinations on the sample calcinated at 250 °C with HR of 5 °C min^{-1} for 1 h, as presented in Fig. 2(a), revealed no detectable crystallographic transformations. This remained unchanged even when the

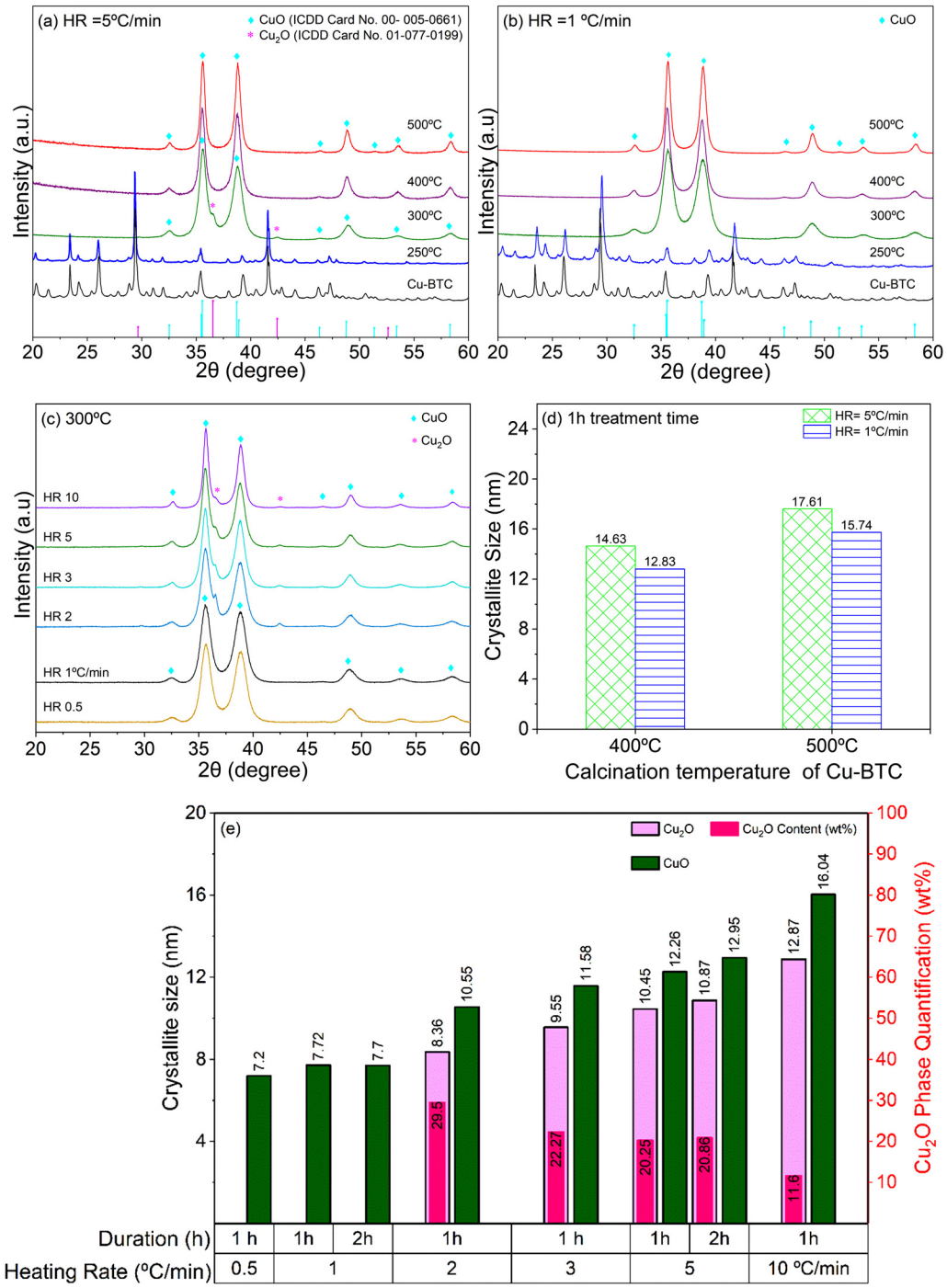

Fig. 2 (a) and (b) XRD patterns of Cu-BTC-derived samples synthesized at different calcination temperatures (T_C) with the heating rate (HR) of 5 °C min^{-1} (a) and 1 °C min^{-1} (b), for 1 h duration. (c) XRD patterns of P-CuO_x synthesized at T_C of 300 °C (for 1 h) with different HR. (d) Crystallite size of P-CuO synthesized at T_C of 400 and 500 °C for 1 h, comparing those treated with different HR (5 °C min^{-1} and 1 °C min^{-1}). (e) Crystallite sizes of CuO and Cu_2O phases and the quantification of Cu_2O for the P-CuO_x synthesized at 300 °C at different HR and durations.

treatment duration was extended to 2 h, as shown in Fig. S2a (ESI,† Section S2), where all diffraction peaks were consistent with those of Cu-BTC (ICDD card 00-065-1028),[25] affirming the stability of Cu-BTC under these conditions. However, raising the T_C to 300 °C initiated a notable phase transition, where the diffraction patterns indicated the transformation of Cu-BTC into a mixed phase of P-CuO$_x$ (Fig. 2(a)). The two phases, cuprous oxide (Cu_2O) and cupric oxide (CuO), were observed for both durations of 1 h and 2 h, as shown in Fig. S2b (ESI†). All diffraction peaks matched well in position and intensity with ICDD card no. 00-005-0661 and ICDD card no. 01-077-0199 for CuO and Cu_2O respectively. Upon elevating the T_C, to 400 and 500 °C, the XRD patterns indicated a complete transformation of Cu-BTC into single phase P-CuO (Fig. 2(a)). The characteristic peaks appeared at 2θ values of 32.5°, 35.4°, 38.7°, 46.3°, 48.7°, 51.3°, 53.4°, and 58.3° correspond to the (110), (−111), (111), (−112), (−202), (112), (020), and (202) crystal planes respectively and consistent with ICDD card no. 00-005-0661 of CuO.

Given the observed stability of Cu-BTC at 250 °C and the phase transitions noted at 300 °C, it became crucial to identify the exact temperature at which complete transformation to copper oxides occurs. To pinpoint this temperature within this range of 250 °C to 300 °C, additional XRD studies were conducted for Cu-BTC-derived samples synthesized at 270 °C and 285 °C with the heating rate (HR) of 5 °C min^{-1} for 1 h duration. The XRD results (Fig. S3 ESI,† Section S2), revealed that complete transformation of Cu-BTC to copper oxides was achieved at approximately 285 °C, marking a definitive phase change.

A reduction in the HR to 1 °C min^{-1} altered the diffraction patterns slightly, as illustrated in Fig. 2(b). While the phase composition of the sample calcinated at 250 °C remained to be Cu-BTC (also, see Fig. S2e, ESI†), a notable change in the diffraction patterns was observed for samples treated at 300 °C. Unlike the rapid HR of 5 °C min^{-1}, the Cu_2O phase disappeared in the obtained structure. However, there was a significant change in the crystallite size as will be described later. The presence of single phase CuO was observed exclusively at the higher T_C of 400 and 500 °C. To address the challenge with achieving pure phase CuO with high crystallinity, especially noted with sample of 300 °C with HR of 1 °C min^{-1}, a stepped heat treatment was conducted. The temperature was initially increased to 300 °C at HR of 1 °C min^{-1} and held for 1 h, then raised to 500 °C under the same HR and kept for another 1 h. The diffraction patterns showed only CuO phase with sharp peaks, as shown in Fig. S4 (ESI,† Section S2).

The preliminary observations from the XRD patterns for the lower HR of 1 °C min^{-1} exhibited distinct features compared to the faster HR of 5 °C min^{-1}, suggesting the profound impact of HR on phase transformation. Following these findings, further experimentations were conducted for more investigation of the transformation, phase composition and quantification of samples treated at 300 °C. These experiments were carried out with different HR: 0.5, 1, 2, 3, 5, and 10 °C min^{-1} for 1 h (Fig. 2(c)). At an even lower HR of 0.5 °C min^{-1}, the sample exhibited a single phase CuO structure, consistent with the behaviour observed at 1 °C min^{-1}. In contrast, Coexistence of CuO and Cu_2O phases was observed with HR of 2 °C min^{-1} and for all other faster HR. Notably, the crystallite sizes exhibited marked variations across the different rates, underscoring the significant impact of heating dynamics on crystallite morphology and overall structural integrity.

The crystallite sizes of the synthesized P-CuO at T_C of 400 and 500 °C were rigorously evaluated using XRD, with analysis based on the main peak CuO (−111). The full-width half maximum (FWHM) of the peak was measured, and Debye–Scherrer formula,[26] as indicated in eqn (1), was applied.

$$D = \frac{k\lambda}{\beta \cos \theta} \quad (1)$$

where D is the crystallite size, K is the shape factor (usually taken as 0.9[27]), λ is the wavelength of the incident X-ray radiation (λ = 0.15406 nm), β is the FWHM, and θ is the Bragg's angle. Analysis revealed that the crystallite sizes of the synthesized P-CuO$_x$ changed by T_C and HR, as presented in Fig. 2(d). Interestingly, variation in size due to changes in the duration was minimal. For example, samples calcinated at 400 and 500 °C with a rapid HR of 5 °C min^{-1} for 1 h, crystallite sizes were 14.63 nm and 17.61 nm, respectively. These sizes slightly increased to 14.89 nm and 17.75 nm when the duration was extended to 2 h, as shown in Fig. S5 (ESI,† Section S2). Conversely, a slower HR of 1 °C min^{-1} for 1 h resulted in smaller crystallite sizes of 12.83 nm and 15.74 nm at 400 and 500 °C respectively, with marginal growth to 12.91 nm and 15.79 nm for 2 h. However, a further reduction in HR to 0.5 °C min^{-1} resulted in no significant change in crystallite size compared to the sample treated at 1 °C min^{-1}, as shown Fig. S6 (ESI,† Section S2). These findings underscore the impact of the heating dynamics on crystallite growth, where the rapid rate promoted larger crystallite size. This was widely investigated for the sample calcinated at 300 °C for both existing phases, Cu_2O and CuO, as shown in Fig. 2(e). The crystallite size of CuO measured 7.72 nm at an HR of 1 °C min^{-1} and decreased slightly to 7.2 nm when the HR was lowered further to 0.5 °C min^{-1}, emphasizing the role of slower heating in reducing crystallite size. In contrast, increasing the HR to 10 °C min^{-1} led to substantial growth, with the crystallite size of CuO reaching 16.04 nm under the same duration of 1 h calcination. The same phenomenon occurred for the Cu_2O phase, where the crystallite size at duration of 1 h increased from 8.36 nm at 2 °C min^{-1} to 12.87 nm at 10 °C min^{-1}. Increasing the heating duration from 1 h to 2 h slightly changed the crystallite size as recorded at HR of 1, and 5 °C min^{-1}.

In terms of phase quantification, the pure CuO was the dominant phase for the samples calcinated at elevated T_C of 400, and 500 °C. Only samples treated at 300 °C showed mixed phases of Cu_2O and CuO at different HR except at 1 °C min^{-1}. The proportions of these phases were quantitatively assessed by analyzing the intensity of the characteristic diffraction peaks for CuO(−111) and Cu_2O(111) planes, using the relative ratio formula: Cu_2O% equals to $I_{Cu_2O(111)}/(I_{Cu_2O(111)} + I_{CuO(-111)})$.[28]

This analysis, as depicted in Fig. 2(e), presented the percentages of the Cu_2O for the samples treated at 300 °C. It was observed that the highest content Cu_2O was 29.5 wt% and recorded with the rate of 2 °C min^{-1} for 1 h. Notably, this percentage decreased to be 11.6 wt% with raising the HR at 10 °C min^{-1}. Extending the treatment duration from 1 h to 2 h resulted in a marginal impact to the content of the Cu_2O phase in the sample. As noted with HR of 5 °C min^{-1}, the percentage slightly increased from 20.25 wt% at 1 h to 20.86 wt% at 2 h.

3.2. TGA analysis

While XRD provided insights about the crystal structure of MOF-derived copper oxides, it was essential to understand the thermal decomposition behavior that guided our heat treatment process. This understanding came from our preliminary TGA study that was complemented with differential thermogravimetry (DTG) analysis, offering deeper understanding for the thermal decomposition behavior of Cu-BTC. TGA was conducted from 25 to 600 °C with HR of 5 °C min^{-1} in air environment, as shown in Fig. 3(a). TGA revealed two main weight losses during the decomposition of Cu-BTC. The initial weight loss (~10.5%) was observed between 40–135 °C which corresponds to the removal of the water and some volatile organic components from the structure of Cu-BTC, and DTG analysis showed that the maximum rate of weight loss happened around 96.5 °C. The second and most-significant weight loss was observed between 285–335 °C, where approximately 66.4% of the initial mass was lost. This massive decrease is due to the breakdown of the Cu-BTC structure. In this stage, DTG displayed a high rate of weight loss around 297 °C, which corresponds to breaking of carboxyl groups (–COOH) from the benzene ring. Subsequently, some gases such as CO_2, CO, and water vapor could be released from the structure. The removal of carboxyl groups led to the formation of copper oxides Cu_2O and CuO increasing the temperature led to the total decomposition of the ligand BTC with the highest weight loss rate that indicated by the sharp DTG peak at 320 °C. Beyond this, no noticeable thermal decomposition or weight loss was observed, indicating the complete decomposition of Cu-BTC structure and its transformation into Cu_2O and CuO. A very slight weight gain of approximately 1% was observed around 400 °C. The weight gain is significantly low making it difficult to draw a definitive conclusion. Upon closer inspection, the increase occurs gradually between 350 °C and 520 °C before levelling off. This indicates that within this temperature range the complete phase transformation takes place resulting the formation of pure phase CuO. This observed weight increase could be attributed to a slow oxygen uptake during the oxidation process, where Cu_2O transforms into CuO and maintained as a single phase.[29–31]

Guided by TGA profile of Cu-BTC, the heat treatment was strategically carried out across a specific range of T_C as previously described. To accurately quantify the effect of this thermal treatment, each sample was precisely weighed before and after treatment, allowing for the determination of exact weight loss, as shown in Fig. 3(b). The measurements revealed that at 250 °C, all samples showed weight loss around 12%, accordance with the removing of water from the structure. All samples at T_C of 300, 400, and 500 °C showed weight loss around 68%, closely aligning with the weight loss observed during TGA analysis.

3.3. Microstructural and compositional analysis

The morphological characteristics of the precursor Cu-BTC and the synthesized P-CuO_x at different T_C for 1 h duration were studied by SEM. As presented in Fig. S7 (ESI,† Section S2), Cu-BTC with an average particle size of 35 μm (Fig. S7a–c, ESI†), displayed a well-defined octahedral crystalline structure. Upon calcination at 250 °C, as observed in Fig. S7d (ESI†), the sample still have the original shape of the Cu-BTC (Fig. S7c, ESI†). Remarkably, SEM analysis of P-CuO_x across all the temperatures tested, with higher magnification insets (Fig. 4), revealed the preservation of the octahedral morphology inherent to Cu-BTC. Samples treated at 300 °C with faster HR of 5 °C min^{-1} showed slight changes from the well-defined octahedral shape, as shown in Fig. 4(a), compared to the slower HR of 1 °C min^{-1}

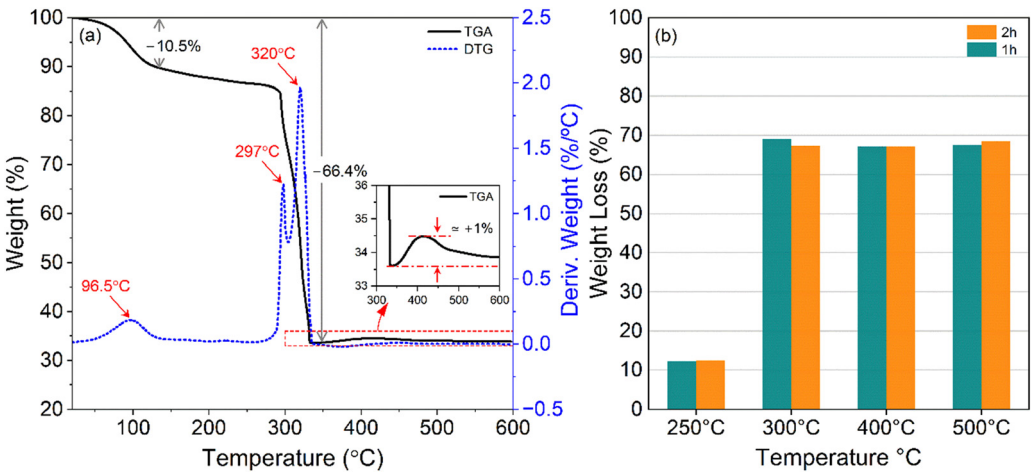

Fig. 3 (a) TGA and DTG of Cu-BTC in air. (b) Calculated weight loss of heat-treated Cu-BTC.

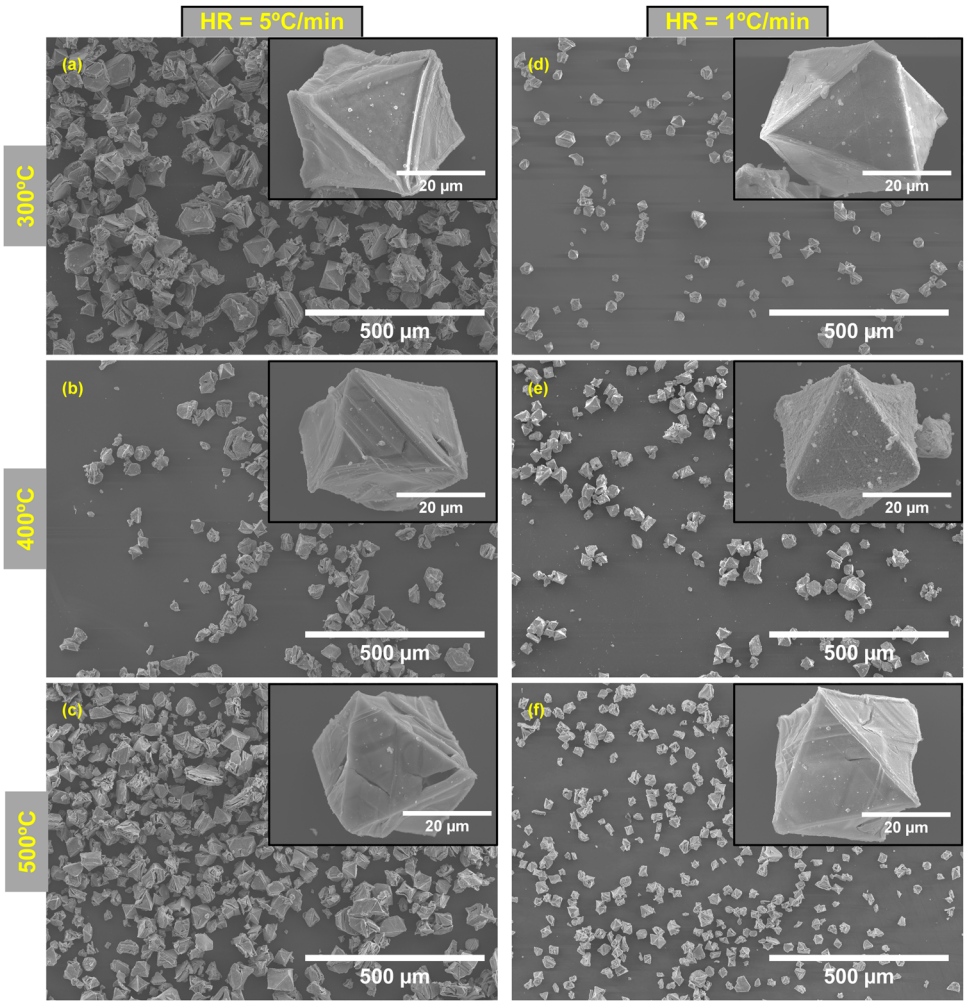

Fig. 4 SEM of the synthesized P-CuO_x at 300 °C (a) and (d), 400 °C (b) and (e), and 500 °C (c) and (f), for 1 h duration, With HR of 5 °C min^{-1} (left column) and 1 °C min^{-1} (right column).

in Fig. 4(d), which retained more of the original shape of parent Cu-BTC MOF with shape features and more defined edges. Increasing the temperature T_C to 400 and 500 °C with 5 °C min^{-1} resulted in more morphological changes (Fig. 4(b) and (c)) compared to a slower HR of 1 °C min^{-1} (Fig. 4(e) and (f)). Magnified SEM images (Fig. S8a and b, ESI,† Section S2) displayed that the obtained P-CuO was porous and composed of large numbers of CuO nanoparticles with size less than 100 nm, assembled forming a nanoporous structure. Also, Fig. S8c–f, ESI,† presented SEM images showing the internal morphology of the synthesized P-CuO.

EDX analysis, complemented with elemental mapping (Fig. S9 and S10, ESI,† Section S2), provided quantitative insights into the elemental composition of the samples. This elemental analysis was applied to the heat-treated samples at HR of 5 °C min^{-1} for 1 h duration. As inferred from the mapping of Cu-BTC, Fig. S9a, ESI,† the elements detected were C, O, and Cu with atomic concentrations of 59.2, 34, and 6.8% respectively. As expected, a high carbon content that attributed to the ligands, compared to the lower copper content that matches with the metal ions. The observed high oxygen content was consistent with the carboxylate groups in the ligands as well as the adsorbed water within the structure. After calcination at 250 °C (Fig. S9b, ESI†), the carbon content remained relatively unchanged, while a noticeable decrease in the oxygen content was recorded alongside with increase in copper content. This reduction in the oxygen amount is due to removal of the water from the structure. Upon elevating at 300 °C (Fig. S10a, ESI†), EDX analysis detected only O, and Cu that constituent about 57.6, and 42.4% respectively, indicating the complete transformation of Cu-BTC into copper oxides and the removal of carbon. Fig. S10b and c, ESI,† presented the same observation for the samples at higher T_C of 400, and 500 °C with marginal changes in oxygen and copper contents. Additionally, elemental mappings for the synthesized P-CuO_x at 300, 400, and 500 °C highlighted a homogeneous distribution for copper and oxygen, demonstrating a uniform transformation of Cu-BTC into copper oxides.

3.4. TEM analysis of the heat-treated Cu-BTC

Based on TGA results complemented with the prior chemical and morphological analysis, calcination of Cu-BTC at T_C of 500 °C for

1 h with HR of 5 °C min^{-1} confirmed the complete transformation of Cu-BTC into a pure CuO phase. Subsequently, this sample underwent further characterization. TEM analysis, as shown in Fig. 5, was carried out for this sample to investigate the nano-structural features of the synthesized CuO. Fig. 5(a) and (b) presented the particle size, and the sample showed particle size mainly in the range of 25–45 nm, with a mean particle size of approximately 31 nm. The selected area electron diffraction (SAED) pattern shown in Fig. 5(c) revealed the characteristics diffraction rings corresponding to the (−111), (111), and (202) crystal planes of CuO. Additionally, the high-resolution lattice-resolved TEM image (Fig. 5(d)) revealed an average interlayer spacing of 0.25 nm (between the lattice fringes), which aligned well to the (−111) lattice planes of monoclinic CuO.

3.5. XPS analysis for chemical state and surface composition

Based on XRD and Raman analysis (ESI,† Section S3) for the thermal-treated Cu-BTC with HR of 5 °C min^{-1} for 1 h duration, distinct phases were identified with mixed phases Cu_2O and CuO for the P-CuO_x synthesized at T_C of 300 °C and a pure CuO phase at 500 °C. Guided by these findings, XPS was employed for further investigation of the chemical state of these samples. Fig. S12 (ESI,† Section S4) showed the survey spectra, which confirmed that the observed peaks were associated with peak elements of carbon, oxygen, and copper. No impurities were detected in the survey spectra. The major contribution for each element in the Cu-BTC and the synthesized P-CuO_x at 300 and 500 °C were recorded in Table S1 (ESI,† Section S4). A high-resolution selected area scans were also recorded for the individual elements of O 1s, and Cu 2p for Cu-BTC, and the samples treated at 300, and 500 °C.

The high-resolution spectra of O1s, as shown in Fig. 6(a), showed one peak for Cu-BTC at 532.6 eV that can be assigned to Cu–O–C species and indicate the presence of carboxylic groups in Cu-BTC.[32–34] For samples of P-CuO_x at 300 and 500 °C, the spectra were decomposed into three peaks at 529, 530.7, and 532.6 eV, and the peak fitting parameters were represented in Table S2 (ESI,† Section S4). The first peak at 529 eV is related to the binding energy of the lattice oxygen O^{2-} in CuO. The other two peaks at 530.7 and 532.6 eV are related to the oxygen species of surface hydroxyls (O–H) and O–C respectively, that adsorbed onto the surface of P-CuO_x.[35]

XPS spectra of Cu 2p, for all samples Fig. 6(b), displayed two main peaks located at 934.8 and 954.6 eV that were associated with the Cu $2p_{3/2}$ and Cu $2p_{1/2}$ respectively. The position of the two peaks matched well with the data recorded in the literature for Cu 2p,[36–38] also the separation of 19.8 eV between the two peaks was the same as in the standard of Cu 2p spectrum.[39,40] The peak's shape was fitted by Gaussian/Lorentzian line-shape (GL30), which was modified by exponential blend to better match the observed data. The results of peak fitting revealed convoluted peaks that attributed to the oxidation state of Cu(II) for all samples. Additionally, the presence of the satellite peaks indicates a partially filled $3d^9$ shell due to the higher oxidation

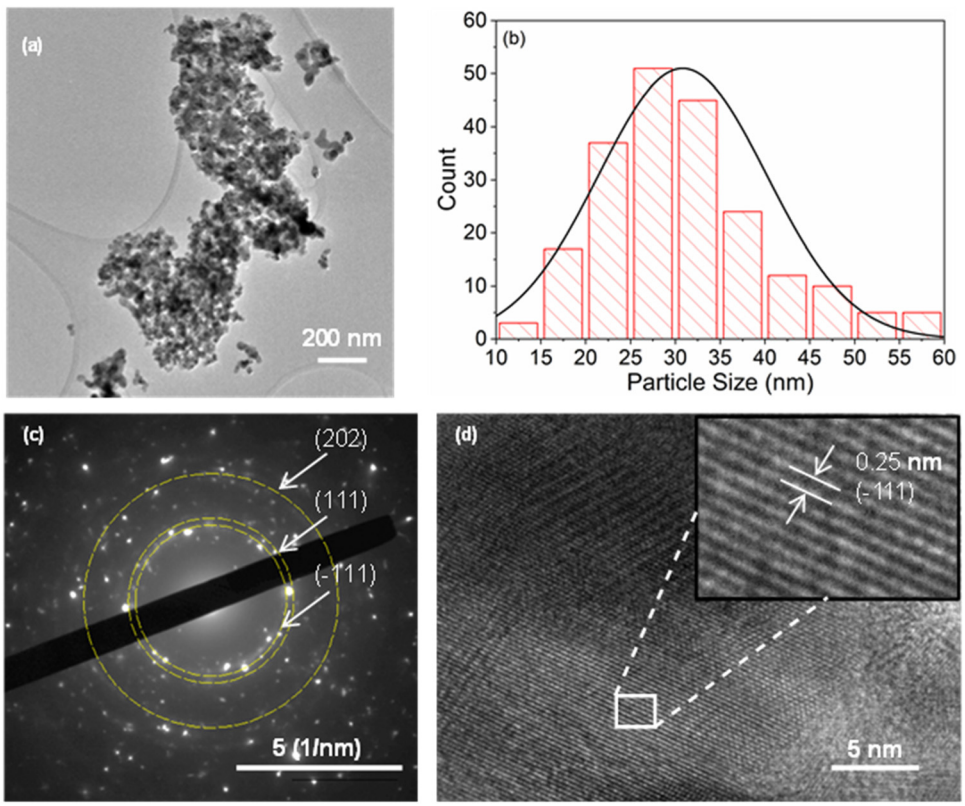

Fig. 5 (a) TEM image of the synthesized P-CuO at 500 °C (with HR of 5 °C min^{-1} for 1 h); and the respective (b) particle size histogram distribution, (c) selected area electron diffraction (SAED) pattern, and (d) lattice-resolved image collected from the region enclosed in a white rectangle.

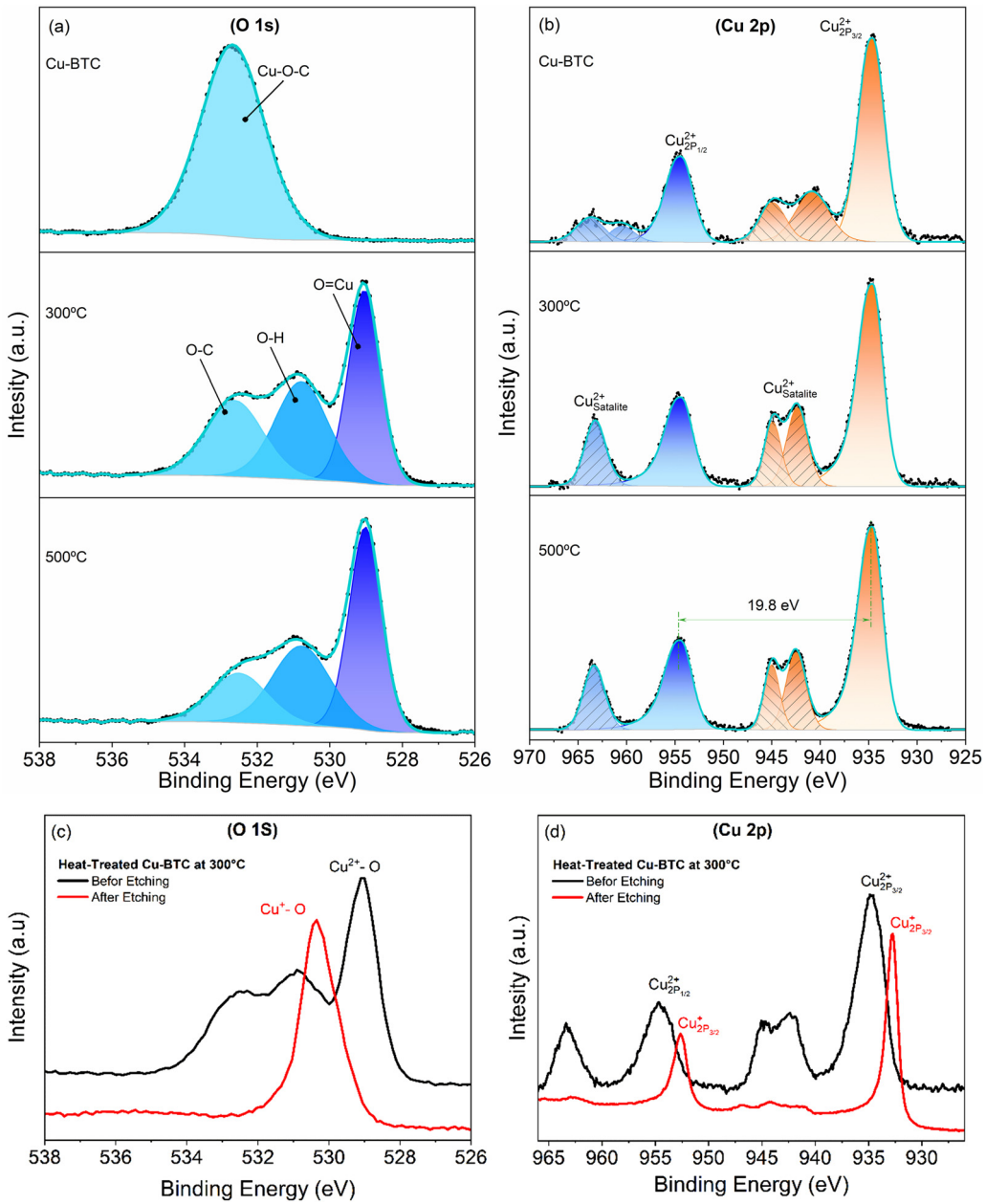

Fig. 6 (a) and (b) High resolution spectrum of O 1s (a) and Cu 2p (b) XPS spectra of pristine Cu-BTC and the synthesized P-CuO_x at 300 and 500 °C (with HR of 5 °C min^{-1} for 1 h). (c) and (d) O 1s and Cu 2p spectra, respectively, for the sample treated at 300 °C after applying ion-beam based surface etching.

state of Cu(II).[37,41] It was noticed that for samples calcinated at 300 and 500 °C, these satellite peaks become strong and positioned at 942.4, 945, and 963.3 eV. The strong satellite peaks provided evidence of Cu(II) oxidation state indicating the existence of CuO phase and negated the likelihood of a Cu_2O phase being present.[42] Regarding the samples treated at 300 °C, according to XRD analysis, both phases CuO and Cu_2O existed. However, XPS spectrum showed only the peak of Cu(II) that consisted with the CuO. The reason for this contrast is that XPS can only get the signal from the surface, not collected from the bulk as achieved in XRD. CuO was the stable phase, therefore CuO phase existed on the surface of the sample instead of having a mixed phase. Consequently, it was concluded that both phases were presented where the CuO is the dominant and stable on the surface, and it could cover or cap the Cu_2O. This was verified by carrying out ion-beam etching based depth profiling on the surface of P-CuO_x at 300 °C. Etching inside the XPS chamber was applied to remove some surface layers, and the underlying layers were analyzed, as shown in Fig. 6(c) and (d). *In situ* etching was conducted for 5 minutes using argon ions (4000 eV, 7 nA beam current, 40° incident angle, and spot size of 500 μm). After etching, O 1s spectrum, Fig. 6(c), showed one peak located at 530.3 eV that related to Cu_2O. Also, the spectrum of Cu 2p, Fig. 6(d), presented only two sharp peaks

located at 932.7, and 952.6 eV that matched with Cu_2O. Interestingly, the satellite peaks vanished providing clear evidence of the absence of CuO. It was observed that CuO disappeared after etching and removing some layers from the surface, suggesting the existence of Cu_2O in the core and CuO at the outer surface. This phenomenon is matched with the literature.[42,43]

3.6. REELS analysis

Understanding the electronic properties of the synthesized P-CuO_x is paramount, especially in the context of its prospective use in nanofluids for solar thermal applications. Band gap particularly serves as a key indicator for the electronic responsiveness and optoelectronic behavior of the material. REELS as shown in Fig. 7, is a powerful tool for more investigation about the electronic structures and was used to get the band gap. Form the low-loss region, as indicated in the insets, the band gap can be precisely determined.[44] This REELS study revealed that the band gap value was E_g = 3.36 eV for Cu-BTC and 1.45 eV for the sample derived at 300 °C. This value for 300 °C is matched with the band gap of CuO as reported in the literature. As the REELS is a surface technique, it was not possible to get the band gap of Cu_2O before etching. However, after etching as shown in Fig. 7(b) the band gap value become 2.07 eV and this value corresponds to Cu_2O.[45] For samples of 400 °C and 500 °C, as presented in Fig. 7(c) and (d), the obtained band gap values were 1.44 and 1.41 eV respectively and these values were well matched with CuO based on literature.[46]

3.7. UPS analysis

To further investigate the electronic structure, UPS was carried out for Cu-BTC, and the sample that calcinated at 500 °C, as shown in Fig. S13 (ESI,† Section S5). The UPS spectra of Cu-BTC revealed on-set and cut-off energies for Cu-BTC at 1.85 and 19.03 eV, respectively, while P-CuO presented corresponding energies of 0.56 and 17.5 eV. The work function (φ) was calculated to be 2.19 and 3.72 eV for Cu-BTC and P-CuO, respectively, as described in the ESI,† Section 5. Additionally, incorporating the band gap (E_g) values from REELS with the Fermi level (E_F) and the valence band maximum (VBM) derived from UPS, the conduction band minimum (E_C) was estimated. These energy levels were utilized to construct the energy band diagram for both Cu-BTC and P-CuO, as depicted in Fig. 8, confirming the p-type semiconductor nature for P-CuO.

3.8. Surface area and porosity analysis

The specific surface area and pore size distribution were investigated, with measurements conducted by nitrogen physisorption at 77 K for pristine Cu-BTC, and the heat-treated samples. Full isotherms of the adsorption–desorption process were recorded to obtain valuable information about pore size and volume. These analysis provided insights into the effects of both T_C and the HR on surface area and porosity. The obtained

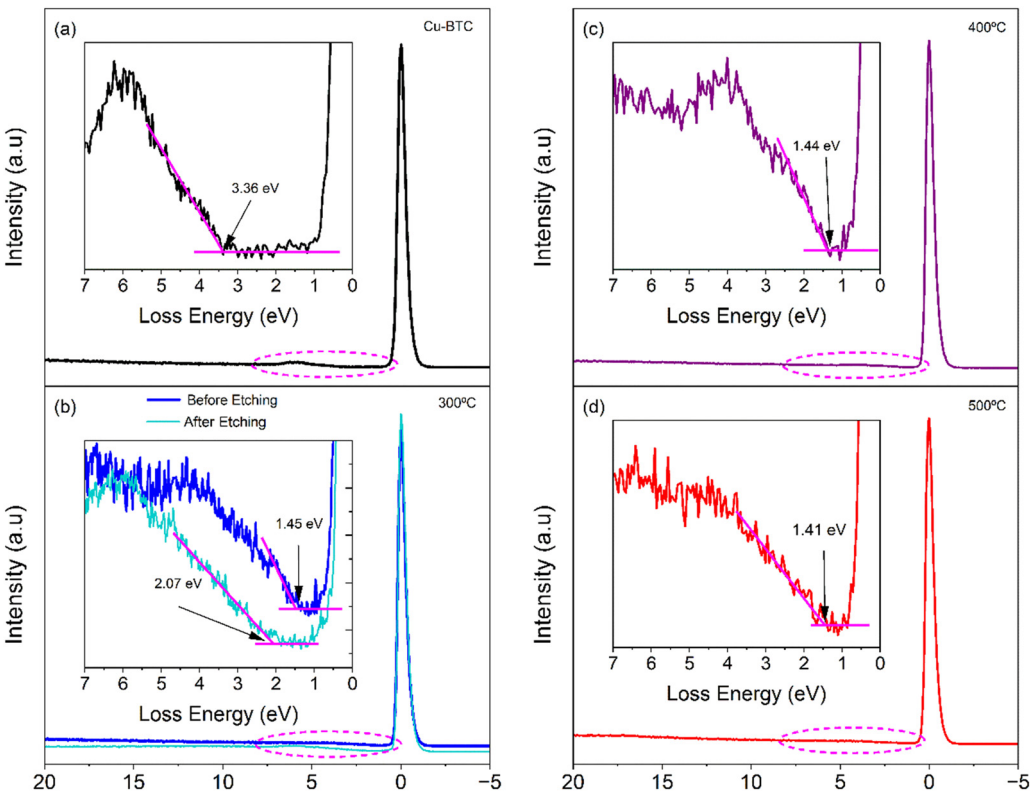

Fig. 7 REELS spectra of (a) pristine Cu-BTC and the P-CuO_x synthesized at (b) 300 °C (before and after surface etching), (c) 400 °C, and (d) 500 °C. Insets display the low-energy loss region, highlighting the band gap transition.

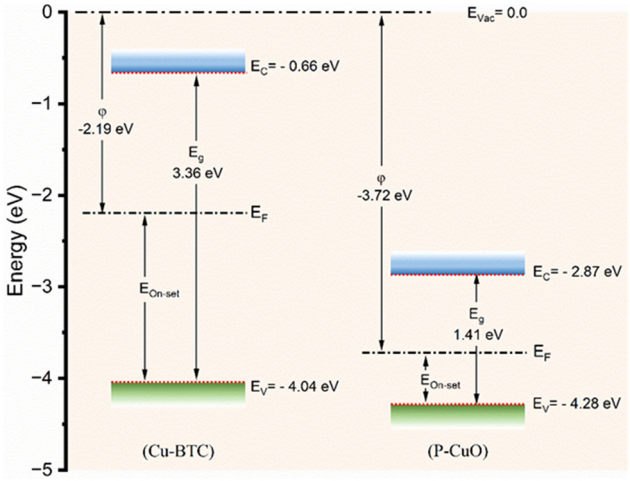

Fig. 8 Energy level band diagram of pristine Cu-BT (left side) and the synthesised P-CuO sample (right side, T_C of 500 °C, HR of 5 °C min^{-1} for 1 h).

full isotherm for all samples, including Cu-BTC (Fig. S14, ESI,† Section S6), and synthesized P-CuO$_x$ (Fig. 9), could be classified as type IV based on the international classification of isotherms.[47] This physisorption isotherm, which plots the volume of gas adsorbed against relative pressure at a constant temperature, was characterized by the adsorption hysteresis loop. This loop, representing the deviation of the desorption curve from the adsorption curve, is associated with capillary condensation occurring within mesoporous structures. type IV with the hysteresis loop implies the mesoporous structure for all samples.

The isotherm for mesoporous structure typically displays an initial rapid increase in adsorbed volume corresponding to the monolayer formation. This is Followed by multilayer adsorption and capillary condensation as the relative pressure increases. With the formation of monolayer, the surface area can be detected over a relative pressure range (p/p^0) of 0.02–0.3,[48] where the p represents the applied pressure of the adsorbate over the sample, and p^0 is the saturation pressure of the adsorbate. Monolayer BET analysis for Cu-BTC presented a high surface area of 1045 m^2 g^{-1}. This surface area significantly decreased for all synthesized P-CuO$_x$ samples, as reported in Tables 1 and 2, indicating the decomposition of the MOF structure. This reduction became more evident with increasing T_C, showing values of 33, 17, and 11 m^2 g^{-1} for the samples treated at 300, 400, and 500 °C, respectively, at HR of 5 °C min^{-1}. The heating rate also had a substantial impact on the surface area. At T_C of 300 °C, the sample treated with a slower HR of 1 °C min^{-1} resulted in a significantly higher surface area of 109 m^2 g^{-1} compared to 33 m^2 g^{-1} achieved with a rapid HR of 5 °C min^{-1} at the same T_C. Even for the sample treated at 500 °C, the slower HR preserved a higher surface area of 25 m^2 g^{-1} compared to 11 m^2 g^{-1} at the faster HR. To explore the effects of an even lower HR, BET surface area measurements were conducted for samples treated at 300 and 500 °C with an HR of 0.5 °C min^{-1} for a duration of 1 h. At 300 °C, the surface area increased from 109 to 113 m^2 g^{-1} when the HR was reduced from 1 °C min^{-1} to 0.5 °C min^{-1}. Similarly, at 500 °C, a slight increase in surface area from 25 to 26 m^2 g^{-1} was observed as the HR decreased from 1 °C min^{-1} to 0.5 °C min^{-1}. The full adsorption–desorption isotherms for these samples were presented in Fig. S15 (ESI,† Section S6). These findings highlight the importance of both T_C and HR in optimizing the surface area during the thermal transformation of Cu-BTC into copper oxides.

Additionally, the hysteresis loops provide insightful information about the pore structure of a material. According to the nitrogen physisorption isotherm of Cu-BTC, where the desorption and adsorption were nearly horizontal and parallel over wide range of p/p^0 (0.5–1), the hysteresis loop could be classified as type H4 which is related to narrow slit-like pores. In contrast, the hysteresis loops for synthesised P-CuO$_x$ samples could be classified as type H3, related to slit-shape pores, without any limiting adsorption at high p/p^0, as verified in Fig. 9. Moreover, the adsorption isotherm of heated-treated samples showed a slight increase in adsorbed volume at a relative pressure lower 0.6 for samples treated at 300 °C, and below 0.85 for those treated at both 400, and 500 °C. Following these thresholds, a significant increase in adsorption was noted, suggesting that the obtained P-CuO$_x$ structure incorporated a wide range of mesopore sizes (2–50 nm). That was verified by presenting the pore width insets in Fig. 9. Pore size distribution and the total cumulative pore volume, noted in Table 1, were analyzed according to density functional theory (DFT).[20,49] This analysis was derived from the amount of gas adsorbed over a range of p/p^0 from 0.15 to near one, and the total volume of pores was obtained at p/p^0 = 0.95. The pore size distribution of pristine Cu-BTC displayed sharp peaks with a narrow range of pore size, suggesting uniformity in pore size with the most common value being 2.6 nm. For the calcinated samples, it was observed that the pore size distribution was impacted by both T_C and HR. At T_C of 300 °C, pore size increased to 12.11 nm, and 8.14 for samples at HR of 5 °C min^{-1} and 1 °C min^{-1}, respectively. For the samples calcinated at 300 °C and 400 °C with a slower HR, pore sizes were mostly below 30 nm, with common sizes being 8.14 nm and 16.68 nm, respectively. However, at T_C of 500 °C regardless of HR, pore size distribution displayed a wide range of pore width over the mesoporous range (<50 nm) and included some macropores range as well.

Calcinated samples at 300 °C, with different HR were investigated for surface area and pore width, as noted in Table 2. The heating rate significantly influenced the surface area and porosity. The surface area dropped from 109 m^2 g^{-1} to 58 m^2 g^{-1} when HR changed from 1 °C min^{-1} to 2 °C min^{-1}. By increasing the HR to 10 °C min^{-1}, the Surface area decreased to 28 with pore size (mode) of 22.12 nm.

3.9. Optical properties

Uv-Vis-NIR spectroscopy was employed to study the optical properties and investigate absorption characteristics of P-CuO$_x$/ethanol dispersion over wavelength range of (300–1400 nm). Absorption and scattering coefficients were studied by measuring

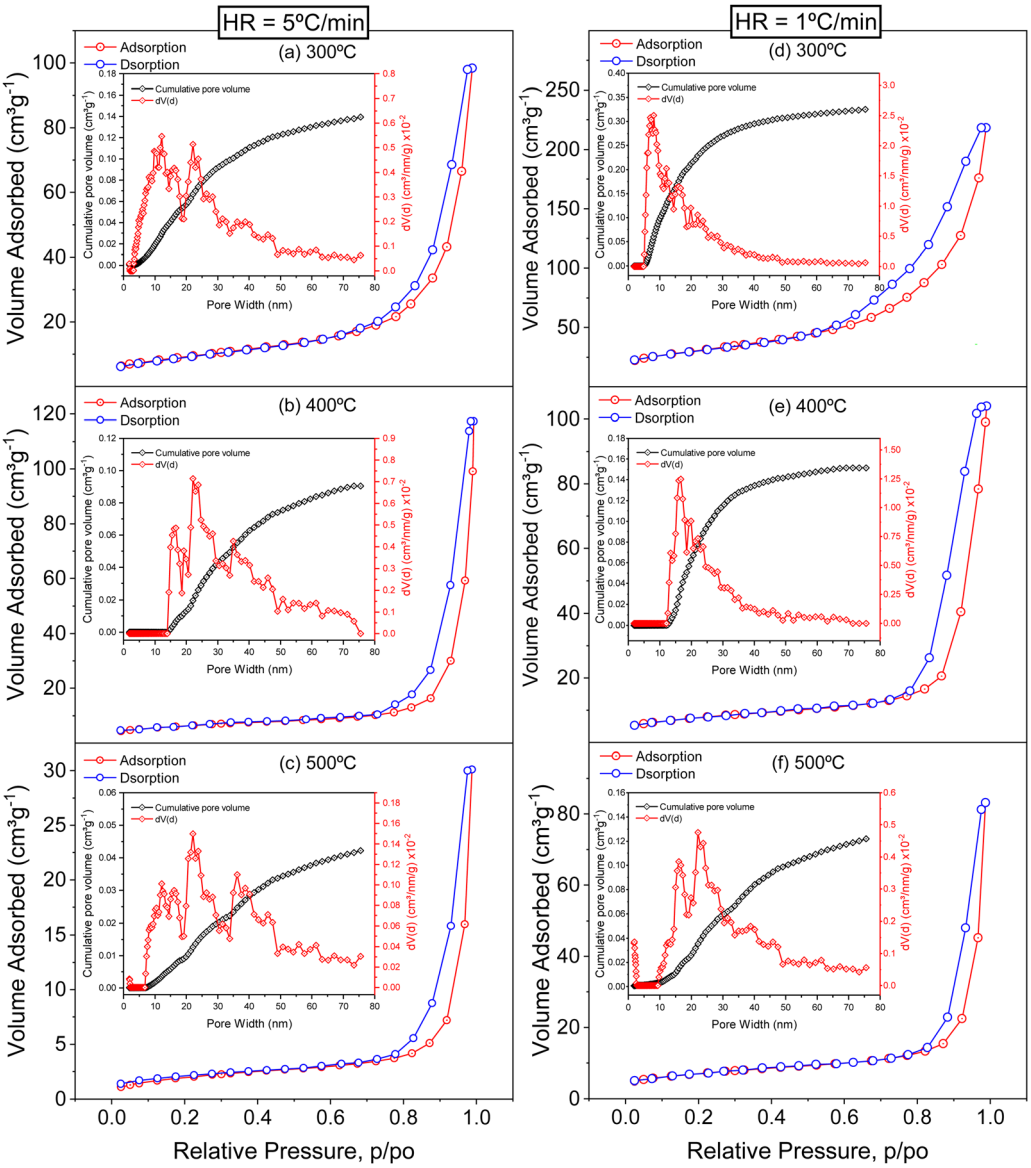

Fig. 9 N_2 Adsorption–desorption isotherms, with insets presenting the corresponding pore size distribution, for the synthesized P-CuO_x at different T_C: (a) and (d) 300 °C, (b) and (e) 400 °C, and (c) and (f) 500 °C, for 1 h duration, with different HR, 5 °C min^{-1} (left column) and 1 °C min^{-1} (right column).

Table 1 Surface area, pore width, and total pore volume for pristine Cu-BTC and the synthesized P-CuO_x at different T_C with different HR for 1 h

HR (°C min^{-1})	Samples	S_{BET} (m^2 g^{-1})	(Mode) pore width (nm)	Pore volume (cm^3 g^{-1})
	Cu-BTC	1045	2.6	0.656
5	250 °C	1020	4.8	0.595
	300 °C	33	12.11	0.139
	400 °C	17	22.12	0.092
	500 °C	11	22.12	0.042
1	250 °C	1035	4.5	0.562
	300 °C	109	8.14	0.325
	400 °C	27	16.68	0.134
	500 °C	25	22.12	0.121

Table 2 BET analysis for the synthesized P-CuO_x at T_C of 300 °C with different HR for 1 h

Sample	HR (°C min^{-1})	S_{BET} (m^2 g^{-1})	(Mode) pore width (nm)	Pore volume (cm^3 g^{-1})
P-CuO_x	0.5	113	8.78	0.434
at 300 °C	1	109	8.14	0.325
	2	58	12.11	0.233
	3	37	12.40	0.150
	5	33	12.11	0.139
	10	28	22.12	0.110

the transmittance, and combined transmittance plus scattering of light pathing through a 10 mm length of the dispersion as described in literature.[50] These coefficients are great ways to illustrate light attenuation due to absorption and scattering respectively within a specific path length. Fig. 10(a), presented

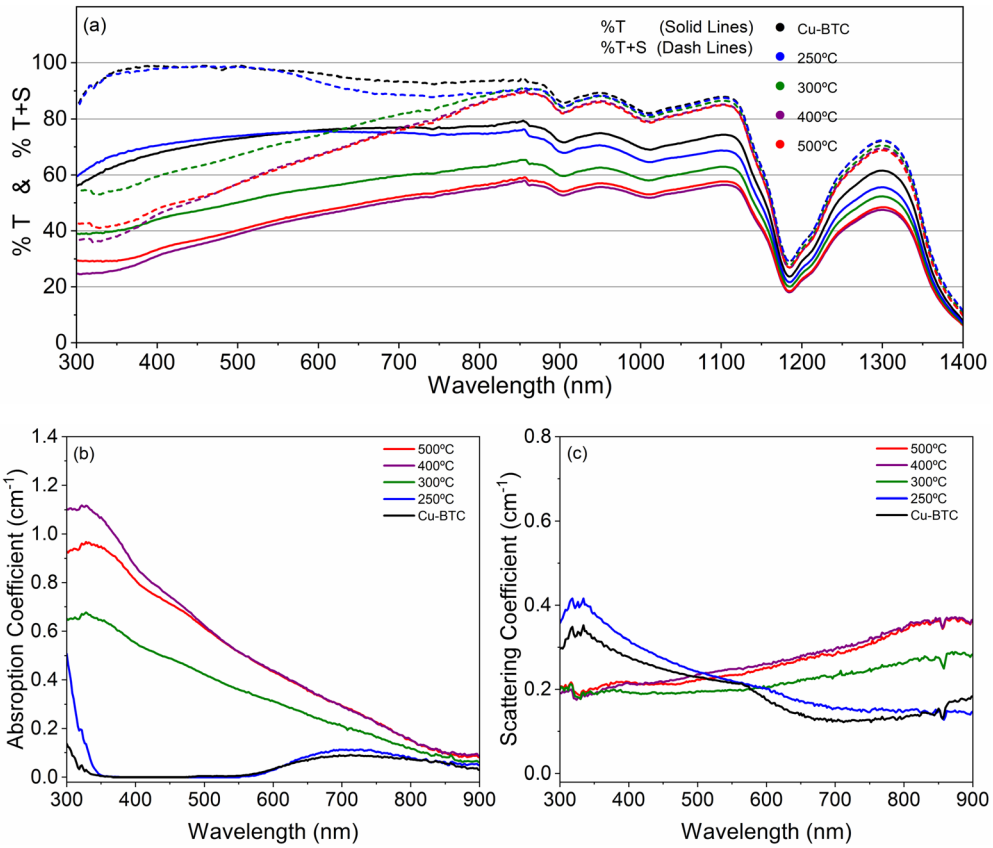

Fig. 10 (a) Transmittance (% T) and transmittance plus scattering (% T + S) of pristine Cu-BTC and the synthesized P-CuO_x at different T_C (HR of 5 °C min^{-1} for 1 h), and the corresponding (b) absorption and (c) scattering coefficients.

transmittance, and transmittance plus scattering for dispersions with 0.02 wt% of Cu-BTC and P-CuO_x samples in ethanol. Absorption and scattering coefficients of all the samples (Fig. 10(b) and (c)) were calculated and presented as a function of wavelength (300–900 nm). Cu-BTC/ethanol exhibited the lowest absorption across the range of interest, particularly below 600 nm, where the absorption coefficient dropped to nearly zero at 550 nm and remained low within the 550 to 350 nm range before increasing at lower wavelength. A similar pattern was observed for the sample calcinated at 250 °C. This weakness in absorption within the range of 550–350 nm is attributed to high scattering in this region, as shown in Fig. 10(c), where the transmittance plus scattering values for both Cu-BTC and the sample calcinated at 250 °C were nearly 100% (Fig. 10(a)), indicating zero absorption. In contrast, P-CuO_x/ethanol demonstrated good absorption coefficients over a wide range of the spectrum. Absorption intensity increased at lower wavelengths, while scattering effect increased at higher wavelengths. Notably, the dispersions with samples treated at 400 and 500 °C, which consist of pure CuO, presented the highest absorption coefficient over the spectrum, with similar values across the spectrum. The 400 °C sample showed higher absorption than the 500 °C sample below 450 nm, which is likely due to its higher surface area of 17 m^2 g^{-1} compared to 11 m^2 g^{-1} for 500 °C sample.

Absorption coefficient can be used to get the band gap according to Tauc plot as described in ESI,† Section S7. Fig. S16 (ESI,† Section S7) presented the value of band gap energy, where Cu-BTC exhibited a band gap of 3.98 eV, which remained unchanged (≈3.97 eV) after calcination at 250 °C. The sample of 300 °C presented two band gap values of 1.51 and 2.11 eV that are consistent with the two phases of CuO and Cu_2O respectively. It was found that the samples of 400 and 500 °C recorded the same value of band gap at around 1.52 eV. In comparison with band gap values obtained from REELS (Fig. 7), it was noticed that the values were quite similar as presented in Table S3 (ESI,† Section S7).

4. Conclusions

This comprehensive study elucidates the transformation process of Cu-BTC into P-CuO_x through controlled calcination, examining the effects of calcination temperature, heating rate, and duration on the phase, morphology, porosity, and optical properties. Through rigorous analysis using XRD, TGA, SEM, BET, and UV-Vis-NIR spectroscopy, we have confirmed that calcination conditions significantly influence the crystallite size, phase purity, and optical characteristics of the synthesized P-CuO_x. The analysis demonstrated that Cu-BTC at lower T_C such as 250 °C maintained its structure, while increasing the T_C to 300 °C initiated a transformation into mixed phases of CuO and Cu_2O. Further elevation

to 400 °C and 500 °C resulted in a complete transition to pure CuO interestingly, specific calcination conditions led to enhanced surface areas with good crystallinity, particularly the stepwise heat treatment process, which involved gradually elevating the temperature from 300 °C to 500 °C at a lower HR of 1 °C min^{-1}, optimize the surface area of P-CuO, achieving up to 42 m^2 g^{-1}. This highlights the potential for optimizing calcination processes to control surface area and porosity without compromising structural integrity. Additionally, the electronic structure of Cu-BTC and P-CuO was explored through REELS and UPS analysis, confirming p-type semiconductor characteristics for P-CuO. The study also highlighted that P-CuO shows optical absorption characteristics over a broader range of wavelength, with high intensity across the visible light range, reinforcing its suitability for solar applications. These comprehensive insights not only advance our understanding of the dynamic transformations within MOF-derived metal oxides but also pave the way for developing advanced nanoporous materials tailored for specific industrial applications.

Author contributions

Sameh Khalil: conceptualization, data curation, formal analysis, investigation, methodology, software, validation, writing – original draft, and writing – reviewing editing. Abhijit Ganguly: data curation, methodology, validation, writing – original draft, and writing – reviewing editing. Davide Mariotti: resources, supervision, and validation. Supriya Chakrabarti: conceptualization, data curation, funding acquisition, investigation, methodology, project administration, resources, supervision, validation, visualization, writing – original draft, and writing – reviewing editing.

Data availability

The data supporting this article have been included as part of the ESI.†

Conflicts of interest

The authors declare no conflict of interest.

Acknowledgements

The authors gratefully acknowledge the support of Ulster University for this research, which was made possible through a funded PhD studentship. S. C. thanks the support of the Department for the Economy (DfE), Northern Ireland, under the US-Ireland R&D Partnership Programme, reference number: USI160.

References

1 S. Polarz and B. Smarsly, *J. Nanosci. Nanotechnol.*, 2002, **2**, 581–612.
2 E. Kianfar and H. Sayadi, *Carbon Lett.*, 2022, **32**, 1645–1669.
3 L. Keshavarz, M. R. Ghaani, O. Saremi and N. J. English, *Adv. Funct. Porous Mater. From Macro to Nano Scale Lengths*, 2022, pp. 319–351.
4 H. J. Jouybari, S. Saedodin, A. Zamzamian, M. E. Nimvari and S. Wongwises, *Renewable Energy*, 2017, **114**, 1407–1418.
5 X. Lang, A. Hirata, T. Fujita and M. Chen, *Nat. Nanotechnol.*, 2011, **6**, 232–236.
6 V. P. Joshi, N. Kumar and R. R. Salunkhe, *Chem. Depos. Nanocrystalline Met. Oxide Thin Film. Synth. Charact. Appl.*, Springer, 2021, pp. 601–621.
7 I. U. Hassan, H. Salim, G. A. Naikoo, T. Awan, R. A. Dar, F. Arshad, M. A. Tabidi, R. Das, W. Ahmed, A. M. Asiri and A. H. Qurashi, *J. Saudi Chem. Soc.*, 2021, **25**, 101228.
8 J. Zhang and C. M. Li, *Chem. Soc. Rev.*, 2012, **41**, 7016–7031.
9 A. Kwiatkowski, J. Smulko, K. Drozdowska, L. Österlund and T. Welearegay, *Sol. Energy Mater. Sol. Cells*, 2024, **273**, 112940.
10 X. Y. Yang, L. H. Chen, Y. Li, J. C. Rooke, C. Sanchez and B. L. Su, *Chem. Soc. Rev.*, 2017, **46**, 481–558.
11 X. Huang, G. Zhao, G. Wang and J. T. S. Irvine, *Chem. Sci.*, 2018, **9**, 3623–3637.
12 A. Feinle, M. S. Elsaesser and N. Hüsing, *Chem. Soc. Rev.*, 2016, **45**, 3377–3399.
13 W. Xiao, S. Yang, P. Zhang, P. Li, P. Wu, M. Li, N. Chen, K. Jie, C. Huang, N. Zhang and S. Dai, *Chem. Mater.*, 2018, **30**, 2924–2929.
14 X. Wang, J. Feng, Y. Bai, Q. Zhang and Y. Yin, *Chem. Rev.*, 2016, **116**, 10983–11060.
15 Y. Wang, Y. Lü, W. Zhan, Z. Xie, Q. Kuang and L. Zheng, *J. Mater. Chem. A*, 2015, **3**, 12796–12803.
16 R. R. Salunkhe, Y. V. Kaneti and Y. Yamauchi, *ACS Nano*, 2017, **11**, 5293–5308.
17 S. Yang, L. Peng, S. Bulut and W. L. Queen, *Chem. – Eur. J.*, 2019, **25**, 2161–2178.
18 Y. Song, X. Li, C. Wei, J. Fu, F. Xu, H. Tan, J. Tang and L. Wang, *Sci. Rep.*, 2015, **5**, 8401.
19 A. F. Payam, S. Khalil and S. Chakrabarti, *Small*, 2024, **20**, 2310348.
20 P. Pang, H. Han, L. Hu, C. Guo, Y. Gao and Y. Xie, *J. Nat. Gas Sci. Eng.*, 2021, **94**, 104060.
21 A. Venkadesh, J. Mathiyarasu and S. Radhakrishnan, *Inorg. Chem. Commun.*, 2021, **128**, 108573.
22 P. Wang, C.-H. Gong, A.-Y. Tang, A.-T. Gu, K.-W. Chen and Y. Yi, *Mater. Res. Express*, 2023, **10**, 25005.
23 N. Nasihat Sheno and A. Morsali, *Int. J. Nanosci. Nanotechnol.*, 2012, **8**, 99–104.
24 T. Feng, Y. Wang, Y. Wu, D. M. Kabtamu, K. Laszlo and F. Li, *J. Mater. Chem. A*, 2020, **8**, 8678–8683.
25 G. A. Bodkhe, B. S. Hedau, M. A. Deshmukh, H. K. Patil, S. M. Shirsat, D. M. Phase, K. K. Pandey and M. D. Shirsat, *Front. Chem.*, 2020, **8**, 1–11.
26 A. L. Patterson, *Phys. Rev.*, 1939, **56**, 978–982.
27 S. A. Disha, M. Sahadat Hossain, M. L. Habib and S. Ahmed, *Results Mater.*, 2024, **21**, 100496.
28 Y. Yang, H. Dong, Y. Wang, C. He, Y. Wang and X. Zhang, *J. Solid State Chem.*, 2018, **258**, 582–587.

29 Z. Lin, D. Han and S. Li, *J. Therm. Anal. Calorim.*, 2012, **107**, 471–475.
30 J. Naktiyok and A. K. Özer, *Niğde Ömer Halisdemir Üniversitesi Mühendislik Bilim. Derg.*, 2019, vol. 8, pp. 1292–1298.
31 A. Domán, J. Madarász and K. László, *Thermochim. Acta*, 2017, **647**, 62–69.
32 X. Li, H. Liu, X. Jia, G. Li, T. An and Y. Gao, *Sci. Total Environ.*, 2018, **621**, 1533–1541.
33 M. B. Nguyen, V. T. Hong Nhung, V. T. Thu, D. T. Ngoc Nga, T. N. Pham Truong, H. T. Giang, P. T. Hai Yen, P. H. Phong, T. A. Vu and V. T. Thu Ha, *RSC Adv.*, 2020, **10**, 42212–42220.
34 P. Gao, X. Y. Sun, B. Liu, H. T. Lian, X. Q. Liu and J. S. Shen, *J. Mater. Chem. C*, 2018, **6**, 8105–8114.
35 J. Yuan, J. J. Zhang, M. P. Yang, W. J. Meng, H. Wang and J. X. Lu, *Catalysts*, 2018, **8**, 171.
36 A. S. Ethiraj and D. J. Kang, *Nanoscale Res. Lett.*, 2012, **7**, 1–5.
37 R. A. Zarate, F. Hevia, S. Fuentes, V. M. Fuenzalida and A. Zúñiga, *J. Solid State Chem.*, 2007, **180**, 1464–1469.
38 W. Lv, L. Li, Q. Meng and X. Zhang, *J. Mater. Sci.*, 2020, **55**, 2492–2502.
39 J. Chastain and R. C. King Jr, *Handbook of X-ray photoelectron spectroscopy*, PerkinElmer Corp., 1992, vol. 40, p. 221.
40 A. Amri, K. Hasan, H. Taha, M. M. Rahman, S. Herman, Andrizal, E. Awaltanova, I. Wantono, H. Kabir, C.-Y. Yin, K. Ibrahim, S. Bahri, N. Frimayanti, M. A. Hossain and Z.-T. Jiang, *Ceram. Int.*, 2019, **45**, 12888–12894.
41 A. Sahai, N. Goswami, S. D. Kaushik and S. Tripathi, *Appl. Surf. Sci.*, 2016, **390**, 974–983.
42 Z. H. Gan, G. Q. Yu, B. K. Tay, C. M. Tan, Z. W. Zhao and Y. Q. Fu, *J. Phys. D: Appl. Phys.*, 2003, **37**, 81.
43 B. Balamurugan, B. R. Mehta and S. M. Shivaprasad, *Appl. Phys. Lett.*, 2001, **79**, 3176–3178.
44 M. Vos, S. W. King and B. L. French, *J. Electron Spectrosc. Relat. Phenom.*, 2016, **212**, 74–80.
45 D. Kovács, A. Deák, G. Z. Radnóczi, Z. E. Horváth, A. Sulyok, R. Schiller, O. Czömpöly and D. Zámbó, *J. Mater. Chem. C*, 2023, **11**, 8796–8807.
46 D. Tahir and S. Tougaard, *J. Phys.: Condens. Matter*, 2012, **24**, 175002.
47 K. S. W. Sing, D. H. Everett, R. A. W. Haul, L. Moscou, R. A. Pierotti, J. Rouquerol and T. Siemieniewska, *Pure Appl. Chem.*, 1985, **57**, 603–619.
48 F. Rechotnek, H. D. M. Follmann and R. Silva, *J. Environ. Chem. Eng.*, 2021, **9**, 106492.
49 N. A. Seaton, J. P. R. B. Walton and N. Quirke, *Carbon*, 1989, **27**, 853–861.
50 H. S. Moghaieb, S. Khalil, A. Ganguly, P. Maguire, D. Mariotti and S. Chakrabarti, *Sol. Energy*, 2024, **273**, 112542.

